

Balancing the Molecular Aggregation and Vertical Phase Separation in the Polymer: Nonfullerene Blend Films Enables 13.09% Efficiency of Organic Solar Cells with Inkjet-Printed Active Layer

Xingze Chen, Rong Huang, Yunfei Han, Wusong Zha, Jin Fang, Jian Lin, Qun Luo,* Zheng Chen, and Chang-Qi Ma

Drop-on demand inkjet-printing (IJP) is a deposition technique with promise in the context of fabricating large-area organic solar cells (OSCs) because of its high material usage, direct-pattern, and large-area roll-to-roll printing compatibility. But its feature of drop-to-drop deposition during IJP makes the film's drying and phase separation process different from spin-coating, and forms different nanophase separation and vertical phase separation morphology. In this work, the nanophase separation of the inkjet-printed organic blend films is systematically studied at different substrate temperatures. The results reveal that increasing the substrate temperature can suppress excess molecules aggregation owing to the high drying speed, leading to improved exciton dissociation efficiency in the blend films. However, the quick drying process at high temperature also leads to a homogenous vertical phase separation, which is not ideal for charge collection. Instead of printing the mixture of donor and acceptor solution directly to form the bulk-heterojunction structure, the polymer donor is printed on the top of the acceptor surface, a so-called layer-by-layer inkjet printing (LBL-IJP) process. By using this LBL-IJP route, balanced nanoscale phase aggregation and gradient vertical phase separation morphology are achieved, which leads to a record power conversion efficiency of 13.09% for the OSCs with an inkjet-printed active layer.

1. Introduction

As an efficient and sustainable energy harvest technology, organic solar cells (OSCs) have attracted extensive attention owing to the benefits of lightweight, semi-transparent, mechanical flexibility, and compatibility with roll-to-roll printing.^[1–4] Recently, due to the development of new photoactive materials and the optimization of photoactive morphology, the power conversion efficiencies (PCEs) of OSCs have exceeded 18%,^[5–9] and the latest record efficiency has reached 19%^[10] for single junction devices. However, these high-performance devices were fabricated by spin coating with a small area of <0.1 cm². The scaling-up fabrication of OSCs that transferring the lab-scale process to large area roll-to-roll printing route would be urgent for the commercialization.^[11]

Among the various printing methods, doctor-blade coating, slot-die coating, gravure printing, and spray coating, inkjet printing exhibits advantages of

direct-patternable, low cost, and saving inks.^[12,13] Inkjet printing is an industrial mature technique used in several conventional fields like book publishing, label, and package printing, etc. Regarding the application of organic electronics, thin and uniform organic films have been fabricated through inkjet-printing (IJP) as well. It reported that inkjet printing is suitable to deposit transparent conduction electrodes,^[14,15] interface buffer layers,^[16,17] and the organic photoactive layers.^[18,19] Thus, fully inkjet-printed OSCs have been successfully fabricated.^[19–22] In addition, inkjet printing can realize the preparation of organic electronics arrays and films fabrication on some unconventional substrates. For instance, Mitra et al. reported the manufacturing of device arrays with different sizes on polyethylene naphthalenediate (PEN) substrate using fully inkjet printing technology. The OSCs arrays based on P3HT:PC₆₁BM have a manufacturing yield exceeded 85%.^[23] Baran et al. successfully fabricated ultrathin solar cells on a 1.7 μm thick perylene substrate through fully inkjet printing. The PCE and power-per-weight of devices reached up to 3.6% and 6.3 W g⁻¹ based on P3HT:O-IDTBR.^[21] The

X. Chen, Y. Han, W. Zha, J. Lin, Q. Luo, C.-Q. Ma
School of Nano-Tech and Nano-Bionics
University of Science and Technology of China
Hefei 230027, China
E-mail: qluo2011@sinano.ac.cn

X. Chen, Y. Han, W. Zha, J. Fang, J. Lin, Q. Luo, C.-Q. Ma
i-Lab & Printable Electronics Research Center
Suzhou Institute of Nano-Tech and Nano-Bionics
Chinese Academy of Sciences
Suzhou 215123, China

R. Huang
Vacuum Interconnected Nanotech Workstation (Nano-X)
Suzhou Institute of Nano-Tech and Nano-Bionics of Chinese Academy of Sciences (CAS)
Suzhou 215123, China

Z. Chen
Shine Optoelectronics (Kunshan) Co. Ltd
Suzhou 215300, China

 The ORCID identification number(s) for the author(s) of this article can be found under <https://doi.org/10.1002/aenm.202200044>.

DOI: 10.1002/aenm.202200044

high power-per-weight of the printed devices showed its potential application of OSCs in space usage^[24] or wearable electronics.^[25]

Since the successful fabrication of the active layers by inkjet printing, many efforts were devoted into the optimization of devices performance through different aspects, such as adjusting molecular regularity,^[26] adding chemical additives,^[16] and using various solvent mixtures.^[18,27–30] In recent years, inkjet-printed OSCs using nonfullerene acceptor (NFA) materials have been reported. Ackermann et al. reported an efficiency of 10.1% based on inkjet-printed PBDB-T-2F:ITIC-4F active layer, which was similar to PCE of the spin-coated device (11.27%).^[30] Baran et al. optimized printing process in inverted architecture, yielding a high PCE of 12.4% and 9.5% for the opaque and semitransparent devices based on PTB7-Th:IEICO-4F bulk heterojunction (BHJ).^[19]

Although the performance of the inkjet-printed OSCs has improved greatly, and several works demonstrated comparable performance of the inkjet-printed OSCs as the spin-coated device for NFA system,^[19,30] the development of OSCs with printed active layer is still lag behind the spin-coated devices. In addition, since most of the previous works on IJP were based on fullerene acceptor system, and relatively few research has been done on non-fullerene systems, the manipulation of morphology for the NFAs based films was rarely studied. We know the drying process during printing is significantly different from the conventional spin-coating process. The films would dry slowly during printing than in spin-coating^[31,32] especially as the solvents used in inkjet printing are always with high boiling point. Thus, when transferring spin-coating to inkjet printing, the regulation of bulk heterojunction (BHJ) morphology becomes more complex and difficult.^[33,34] It has been known that the performance of BHJ OSCs is determined by the phase separation morphology, which is impacted by processing technology and solvent.^[35–37] In fact, slower drying is favorable for high performance P3HT:PCBM devices because P3HT needs relative large and oriented crystalline.^[38] Nevertheless, the NFA-based OSCs usually required quick dry, otherwise excessive aggregates would form and lead to poor performance.^[31,39–41] Thus, it would be more difficult to control the nanostructure and phase separation morphology of the NFA-based blend films, and is extremely challenging to achieve reasonable nanomorphology with weak aggregation that ensure efficient charge separation and transport.^[42] As far as we know, there is rather limited research focused on the investigation of morphology characteristics and manipulation of the inkjet-printed NFA blend films.

In this work, with the aim to prepare high efficiency OSCs with inkjet-printed active layer, the nanophase morphologies of the blend films were systematically investigated and manipulated. First, homogenous and uniform film were obtained via optimizing substrate temperature and drop spacing. Increasing printing temperature had effectively suppressed excess aggregation and improved the crystalline, consequently led to enhanced exciton dissociation. However, increasing printing temperature caused the formation of a homogenous vertical phase separation from surface to bottom, which is adverse for charge collection. To make a balance, layer-by-layer IJP (LbL-IJP) at high temperature strategy was developed. With this optimized

approach, a balanced nano-phase morphology features with a gradient vertical phase separation and acceptable molecular aggregation was achieved. With optimized printing route, a record high efficiency of 13.09% was achieved for OSCs with inkjet-printed active layer.

2. Results and Discussion

2.1. Manipulation of Mesoscopic Morphology

Figure 1a,b show the schematic diagram of inkjet printing, and molecular structures of organic donor poly[(2,6-(4,8-bis(5-(2-ethylhexyl)thiophen-2-yl)benzo[1,2-b:4,5-b']dithiophene))-*alt*-(5,5-(1',3'-di-2-thienyl-5',7'-bis(2-ethylhexyl)benzo[1',2'-c:4',5'-c']dithiophene-4,8-dione))] (PBDB-T), and acceptor 3,9-bis(2-methylene(3-(1,1-dicyanomethylene)indanone))-5,5,11,11-tetrakis(4hexylphenyl)-dithieno[2,3-d:2',3'-d']-s-indaceno[1,2-b:5,6-b'] dithiophene (ITIC). As a key factor of inkjet printing, solvents play a decisive role in the film quality and physical properties of the device. Table S1, Supporting Information, showed the typical inks parameters for the CB and oDCB-based inks. Z number, calculated from equation: $Z = Oh^{-1} = Re/(We)^{1/2} = (\rho\gamma\eta)^{1/2}/\eta$ was commonly used to reveal the printability of inks,^[12,13,43] where ρ , γ , and η is density, surface tension and dynamic viscosity of the solution, respectively. For inks with Z number at range of $1 < Z < 10$, it was more suitable for inkjet printing. Based on this, oDCB with Z of 13.16 rather than CB ($Z = 18.68$) was used as solvent in this work.

Mesoscopic morphology of printed thin film is highly important for the printed films since the trace of droplets can last up to 100 μm . As a non-contact printing method, the film deposition and drying behavior of inkjet printing are unlike spin-coating and slot-die coating. During inkjet printing, film is formed through depositing the droplets one by one. Therefore, controlling the droplet separation, fusion, and solvent evaporation behavior are essential to obtain homogeneous functional films in inkjet printing. Herein, we investigated the influence of drop spacing (DS) and substrate temperature on the film quality. As shown in Figure 1c, the films printed with DS of 20 and 30 μm contained some aggregate dots. It is mainly because excessive solvent did not evaporate and films dry slowly at low temperatures, causing self-aggregate dots and pinholes on surface. Printing with 50 and 60 μm DS formed continuous line, but could not form a continuous plane due to large drop spacing. An optimization, high-quality films were obtained when printed with a DS of 40 μm , thereby DS of 40 μm was chosen to print the active layer. Then, with optimized DS of 40 μm , we prepared a series of films at different temperatures, and the optical microscope images showed all the films from different temperatures were homogenous. However, obvious overlap of printing lines was observed in the films from 50 and 60 $^{\circ}\text{C}$, which was because the former printed lines dried before connecting with next line. Though the printed lines did not fuse well in case of high temperature (50–60 $^{\circ}\text{C}$), the micro-morphology of these films were more beneficial for device performance (vide infra).

The atomic force microscopy (AFM) of the PBDB-T:ITIC blend films at different temperatures were investigated and

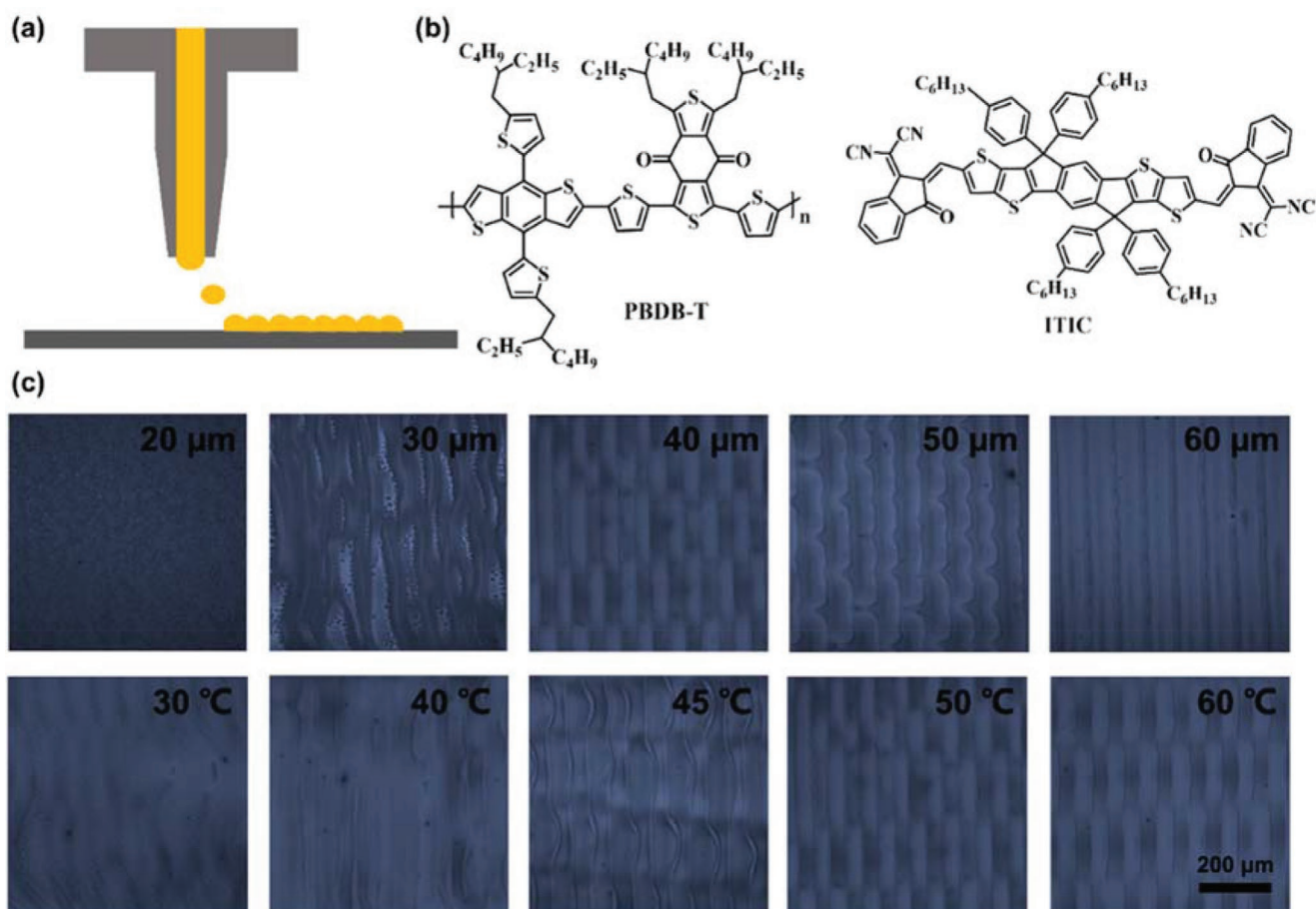


Figure 1. a) A diagram of process of inkjet-printed films. b) Chemical structure of donor and acceptor. c) Optical microscope images of the printed PBDB-T:ITIC blend films. The first row shows the images of blend films printed with different drop spacing at 50 °C, and the second row shows the images of blend films printed with different substrate temperature at a DS of 40 μm. Scale bar = 200 μm.

shown in Figure 2a–h. These films have similar thickness around 140 nm. It can be seen from AFM images that the surface roughness of the films gradually decreased from 6.53 to 3.28 nm when temperature increased from 30 to 60 °C. This could be attributed to restrain of molecular aggregation because of faster drying speed when temperature rising. Meanwhile, it should be noted that the film roughness and aggregation size of the printed films are basically same when substrate temperature increasing from 50 to 60 °C, which leads to similar device efficiency (vide infra). As shown in Figure S1, Supporting Information, the absorption spectra of the inkjet-printed blend layers exhibited a blue shift of the absorption peaks from PBDB-T as temperature increased from 30 °C to 50 °C, which suggested the formation of H type aggregates.^[31,44] Furthermore, the absorption peak of ITIC at 700 nm has stronger intensity with the increases of substrate temperature. This indicates that ITIC molecular forms lamellar stacking.^[45]

To systematically study the films morphology printed at different substrate temperatures, grazing incidence wide-angle X-ray scattering (GIWAXS) was employed to characterize crystallinity of blend films. As shown in Figure 2i–l, the blend films exhibited highly ordered π – π stacking (010) peak around 1.75 \AA^{-1} in out-of-plane (OOP) direction and lamellar stacking

(100) peak around 0.30 \AA^{-1} in in-plane (IP) direction. From 2D GIWAXS pattern images of the printed films, the intensity of lamellar stacking (100) peak and π – π stacking (010) peak were enhanced with increase in temperature. At high temperature of 50 °C, highest diffraction intensity of (010) peak was observed. In addition, we also calculated the stacking spacing and the crystal coherence length (CCL) of blend films according to Scherrer equation.^[46] The fitting curves of different diffraction peaks were shown in Figure S2, Supporting Information. As shown in Table S2, Supporting Information, increasing substrate temperature from 30 to 60 °C has led to increased quantified CCL from 27.38 to 29.35 nm for the OOP (π – π) stacking, the stacking spacing has no obvious change. These results indicated the enhancement of ITIC crystallinity.

2.2. Device Performance of the Inkjet-Printed OSCs

Based on the morphology and crystalline results, we know that temperature increase has suppressed excessive molecular aggregation, resulting in more abundant donor–acceptor (D/A) interfaces. In order to investigate the effect of printing temperature on device performance, a series of OSCs with

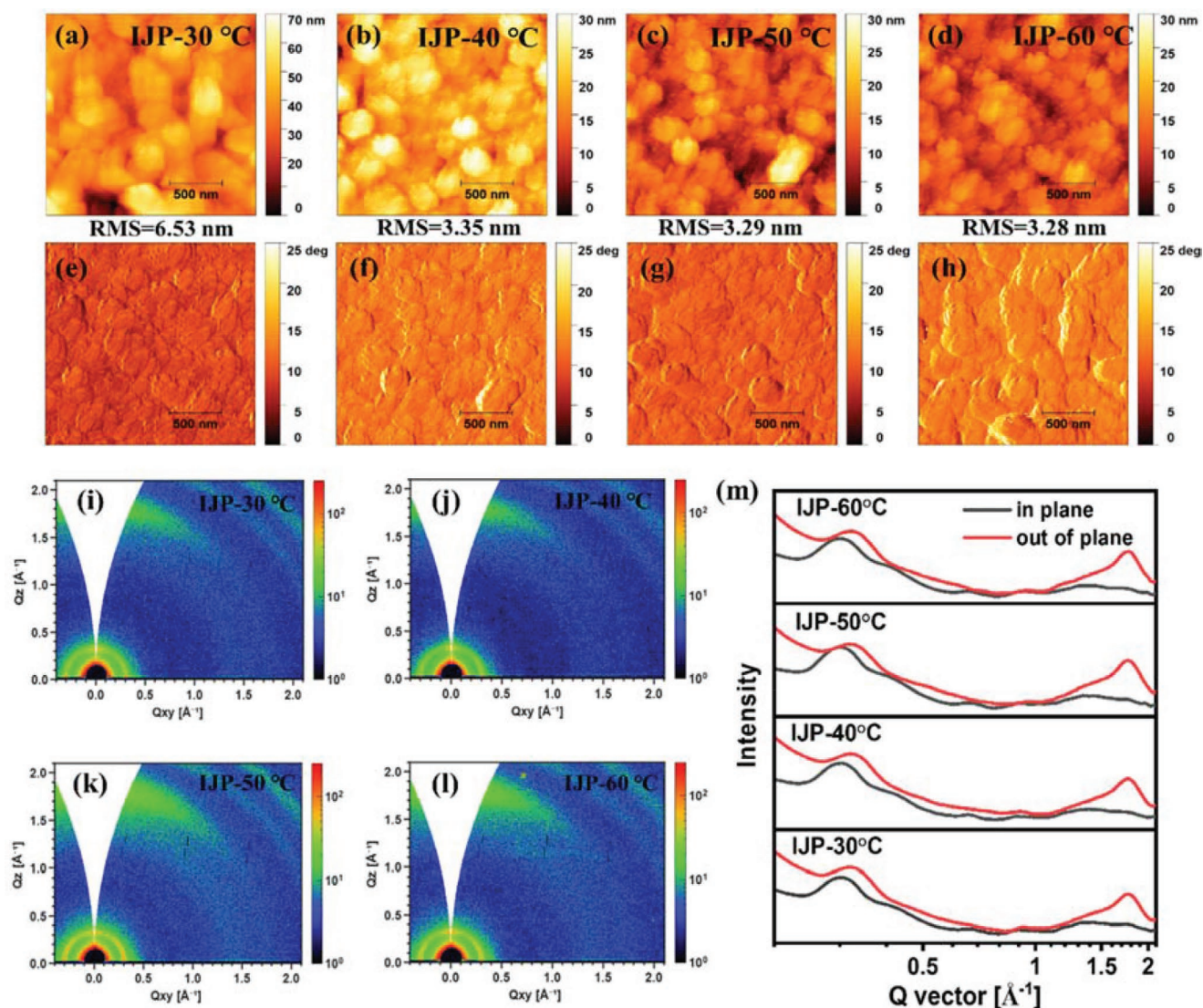


Figure 2. AFM height images (a–d), phase images (e–h) of the PBDB-T:ITIC blend film fabricated from inkjet printing. i–l) 2D GIWAXS patterns and m) line profiles of printed films at different substrate temperatures.

inkjet-printed PBDB-T:ITIC films were fabricated. **Figure 3a,b** shows the device architecture and energy levels of the glass/ITO/ZnO/active layer/MoO₃/Al device. The current density–voltage (*J*–*V*) characteristics and external quantum efficiency (EQE) spectrum of solar cells were measured and shown in **Figure 3c,d**, and the performance parameters were summarized in **Table 1**. Devices from spin-coating were also fabricated as a comparison. The IJP active layers printed from different temperatures have similar thickness around 140 nm, which were slightly thicker than the spin-coated films (120 nm). As showed in **Table 1**, the devices processed by spin coating (SC) showed an average PCE of 8.16%, with an open circuit voltage (*V*_{OC}) of 0.88 V, short circuit current density (*J*_{SC}) of 14.84 mA cm⁻², and fill factor (FF) of 63%. Herein, the devices performance processed by spin-coating was lower than the value reported by references,^[47] which was due to the use of different solvents. The previous reports always used CB as solvent, while here oDCB was used. Then, we observed that OSCs

with inkjet-printed active layer was lower than the SC devices. In addition, printing temperature showed a significant influence on the performance. Specifically, PCEs enhanced from 2.73% to 6.43% when substrate temperature increased from 30 to 60 °C, and *J*_{SC}, FF increased to 13.60 mA cm⁻² and 55%, respectively. The enhanced *J*_{SC} was proved by the EQE spectra, in which the maximum EQE increased from 40% to 60%. As illustrated by the mesoscopic morphology, more uniform and smooth films were obtained with the increase of substrate temperature. In addition, high-temperature printing led to less molecular aggregation and increased crystallization. Thus, the performance improvement could be due to improved crystallization and the passivated molecular aggregation in the films. Similar results have been reported in spin-coated devices as well.^[41,45,48,49] When substrate temperature increased from 50 to 60 °C, *J*_{SC} has a slight reduction from 14.04 to 13.60 mA cm⁻², and FF increased from 53% to 55%. As a consequence, the device processed at 60 °C showed a similar performance as the

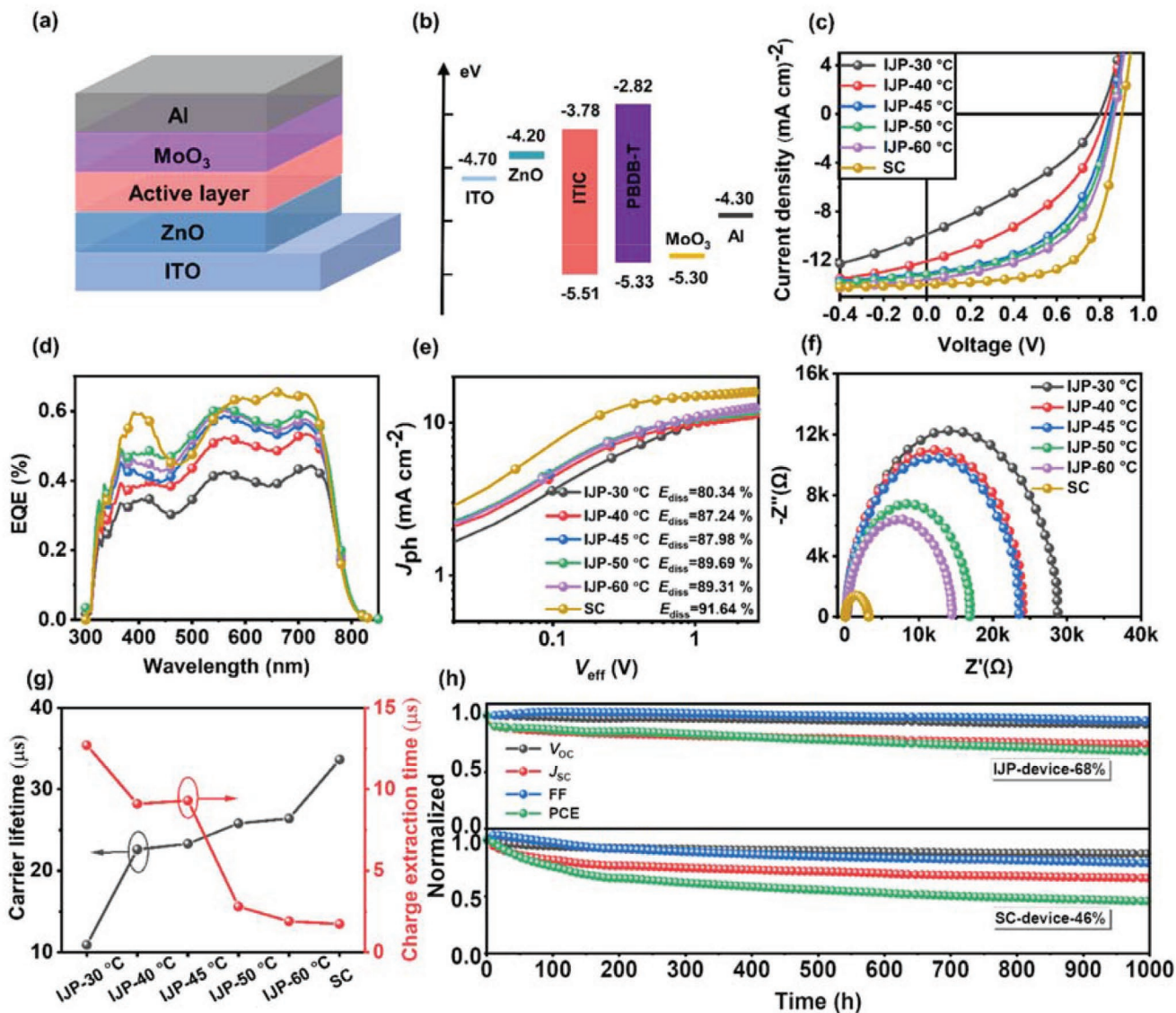


Figure 3. a) Device structure of the inverted OSCs, b) energy level of the inverted OSCs, c) J - V characteristics, d) EQE spectra, e) photocurrent versus effective voltage, f) EIS spectra, g) carrier life, and charge extraction time of the inkjet-printed and coated OSCs that calculated from TPC and TPV. h) Evolution of V_{oc} , J_{sc} , FF, and PCE of the inkjet-printed and spin-coated OCSs during 1000 h continuous illumination.

Table 1. Performance parameters of inverted PBDB-T:ITIC OSCs with active layers fabricated from spin coating and inkjet printing at different deposition temperatures.

Process	Temperature [°C]	Thickness [nm]	V_{oc} [V]	J_{sc} [$\text{mA}\cdot\text{cm}^{-2}$]	FF	PCE ^{a)} [%]
SC	R.T.	118	0.876 (0.872 ± 0.007)	14.84 (14.84 ± 0.12)	0.63 (0.62 ± 0.01)	8.17 (8.16 ± 0.01)
IJP	30	137	0.791 (0.789 ± 0.002)	9.90 (9.64 ± 0.20)	0.35 (0.34 ± 0.01)	2.73 (2.72 ± 0.08)
	40	142	0.829 (0.826 ± 0.003)	12.07 (11.59 ± 0.40)	0.45 (0.44 ± 0.01)	4.51 (4.20 ± 0.31)
	45	140	0.834 (0.834 ± 0.005)	13.12 (13.15 ± 0.35)	0.52 (0.52 ± 0.01)	5.66 (5.45 ± 0.21)
	50	146	0.862 (0.859 ± 0.002)	14.04 (13.70 ± 0.35)	0.53 (0.53 ± 0.01)	6.40 (6.22 ± 0.18)
	60	143	0.863 (0.863 ± 0.001)	13.60 (13.42 ± 0.13)	0.55 (0.54 ± 0.01)	6.43 (6.23 ± 0.20)

^{a)}average PCE was calculated over eight individual devices.

films printed at 50 °C. This may be because the printed film at 50 °C exhibited promoted crystalline as proved by the stronger intensity of π - π stacking (010) peak, which was favorable for charge transfer and transport.

In order to study the effect of printing temperature on the exciton dissociation and charge collection of active layers, we measured the photocurrent density (J_{ph}) versus effective voltage (V_{eff}) (Figure 3e).^[50] Herein, J_{ph} is defined as $J_{ph} = J_L - J_D$, where J_L and J_D represent photocurrent density under AM 1.5G illumination and dark current density, respectively. V_{eff} is defined as $V_{eff} = V_0 - V$, where V_0 is the voltage when photocurrent density $J_{ph} = 0$, and V is the applied voltage on the printed devices. The charge dissociation and collection efficiency (E_{diss}) were calculated according to the ratio of J_{ph}/J_{sat} , where J_{sat} is the J_{ph} at $V_{eff} = 2$ V. As a result, the charge dissociation efficiency increased from 80.34% (30 °C) to 89.69% (50 °C), which could be ascribed to the improved crystalline of the active layer as supported by the GIWAXS results. The electrical impedance spectroscopy (EIS) was performed to investigate the charge transport and recombination process in the printed devices. Figure 3f shows the Nyquist plots of the printed devices. When temperature increased from 30 to 60 °C, the devices plots exhibited smaller semicircles, which revealed lower charge-transfer resistance and better ohmic contact. Then transient photocurrent (TPC) (Figure S3a, Supporting Information) and transient photovoltage (TPV) (Figure S3b, Supporting Information) of these devices were measured to study the charge extraction and carrier recombination processes. We extracted the carrier lifetime and charge extraction time of the OSCs with IJP active layer through mono-exponential decay fitting. As shown by Figure 3g, the devices with active layer printed at higher temperature showed a shorter charge extraction time. And the carrier lifetime steadily increased from 10.9 to 26.4 μ s when substrate temperature increased from 30 to 60 °C. The faster charge collection process and longer carrier lifetime contributed to the enhancement of J_{SC} and FF in the high-temperature printed device.

The long-term stability of the devices with printed and coated active layers was then investigated (Figure 3h). As showed by the evolution of V_{OC} , J_{SC} , FF, and PCE, we found the SC device declined continuously and remained 46% of the efficiency after 1000 h continuous illumination. Among the four performance parameters, degradation of FF and J_{SC} was much faster than that of V_{OC} . The IJP devices were more stable, which remained 68% of the initial efficiency and 96% of initial FF after 1000 h continuous illumination. Our previous work found interfacial photodegradation of organic acceptor due to photocatalysis effect of ZnO could lead to fast J_{sc} decay of OSCs,^[51,52] which was a main reason for the performance decay. Since OSCs both from SC and IJP active layers have identical device structures but different deposition process, the improved operational stability of OSCs with IJP active layer might be ascribed to the more stable nanomorphology of the printed film.

2.3. Inhomogeneous Distribution of Polymer Donor and NFA Acceptor on the Surface

The above results showed the devices with optimized IJP active layer presented a lower performance, but a better

long-term stability. To understand the underlying reasons, we analyzed the nano morphologies of the IJP and SC films using time-of-flight secondary ion mass spectrometry (ToF-SIMS). Chemical mapping with ToF-SIMS allows a deep analysis of the surface composition of solid films based on the secondary ion spectrum of the samples. The cyano (CN) anion was used to describe the distribution of acceptor ITIC in the blend films. Since the amount of S atom in donor is twice that in acceptor, thereby the mapping of S anion can reflect the distribution of donor to some extent. In comparison with spin-coating and some Meniscus-guided coating processes, including slot-die and doctor-blade coating, the film formation process during IJP was quite different. During IJP, the films were formed through droplet coalescence. The adjacent droplets were redissolved or partly redissolved by the subsequent droplets. For the organic donor and acceptor materials with different solubilities, one of the compounds in the blend films would be more re-dissolved by the subsequent droplet, consequently, lead to local composition variation. Thus, for the inks containing D:A mixtures, the droplet coalescence process would be more complex and interesting. To clearly show the droplet coalescence process, we should firstly know the size of the single droplet. So, individual droplets arrays were printed with large DS of 100 μ m to clearly show the size of droplet. The photographs showed the size of individual droplet was around 80 μ m (Figure S4a, Supporting Information). In addition, no obvious coffee ring was observed in the photograph. Knowing the size of individual droplet is 80 μ m, the periodic printing line with width of 40 μ m printed at 40 DS in the optical microscope images (Figure S4b, Supporting Information) could be attributed to drop coalescence rather than coffee ring, which meant the follow-up droplet was half overlapped with the front droplet (as showed by the schematic process described as Figure S4c, Supporting Information). On the basis of these results, we divided the printed films into two different parts, the center and edge of the printed overlap regions. We marked these two parts regions using blue and red line, respectively. As shown in Figure 4a,b, it was clear that the distribution of S was more homogenous than the distribution of CN in the printed films. In the case of CN, there were more CN at the center of printed line than at the edge, indicating ITIC molecules enriched at the droplet center. However, Figure 4c,d showed the distribution of CN and S were uniform in the spin-coated films. To quantifiably show the distribution of donor and acceptor, intensity change of CN and S anion were obtained by integrating the signal intensity perpendicular to the printing direction. With these results, the ratio of CN to S was also calculated. As shown in Figure 4e,f, we can find that the intensity of CN and S exhibited obvious crest and trough in printed films. In contrast, the intensity of CN and S, as well as the intensity ratio of CN/S has no obvious change in the SC films. These results clearly showed an interesting surface phase separation of the IJP films. Specifically, in the direction of printing, donor and acceptor showed a periodical phase separation distribution. Acceptor more tended to enrich at the center of printed lines rather than at the edge, while acceptor was nearly uniform. Such a result might be ascribed to the easier redissolution of acceptor when the adjacent droplets were coalescent, while donor was less redissolution.

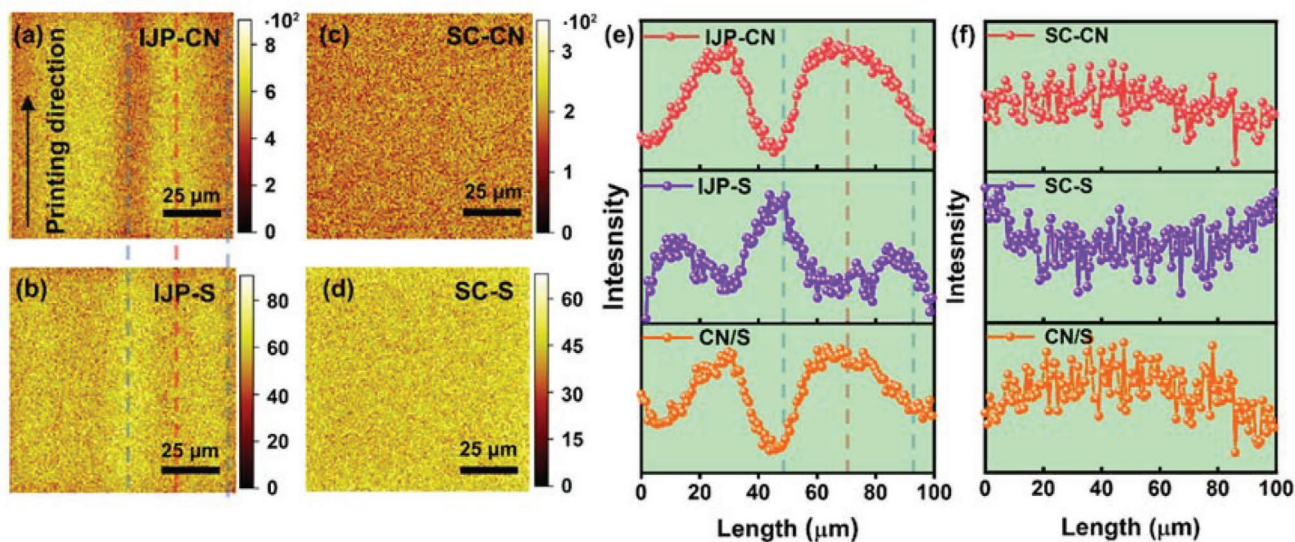


Figure 4. Surface ToF-SIMS mapping of the printed films through printing at 50 °C with DS of 40 μm, and coated films. a,b) The mapping of CN and S of printed film. The printing direction is along the array direction. The red and the blue lines are the center and edges of the overlap region of the neighbor printing lines, respectively. The width of the printed line is 80 μm. Scale bar = 25 μm. c,d) The mapping of CN and S distribution in the coated film. e,f) Intensity change of CN, S anion and CN/S in the printed and coated films perpendicular to the printing direction.

2.4. Vertical Donor: Acceptor Distribution of the Printed Films

Figure 5a,b showed the ToF-SIMS results of the optimized SC and IJP blend films with thicknesses of 120 and 140 nm, respectively. The quantitative change of donor and acceptor in the SC and IJP films clearly showed gradient vertical phase separation in the SC films and homogenous vertical phase separation in the IJP films. In the spin-coated films, the intensity ratio of CN/S gradually reduced from film bottom to surface (Figure 5a), suggesting a gradient vertical component distribution. Specifically, PBDB-T molecular tends to spontaneously distribute on surface, and ITIC molecular tends to distribute at the bottom of active layer. Such a gradient vertical phase separation with donor and acceptor rich at anode and cathode interface has been reported in several previous works.^[53,54] The enrichment of donor at anode, as well the enrichment of acceptor at cathode interface would enable the formation of a continuous pure phase at interface that ensures the exciton dissociation and effective charge transport.^[55] Thus, such a vertical phase separation of the spin-coated films would be beneficial to device performance. However, the intensity ratio of CN/S in the inkjet-printed films almost exhibits no difference at different depths, except a slightly higher intensity ratio of CN/S on the surface of films (Figure 5b). These results suggested negligible enrichment of acceptor and donor, which might be a reason for relative low device efficiency of the IJP OSCs. Then, based on the ToF-SIMS mapping (Figures S5 and S6, Supporting Information), the CN/S ratio at three different depths (surface, depth 1, and depth 2) were shown in Figure 5c,d. It was clear to find the CN/S ratio at different depths kept constant. Whereas, the CN/S ratio was much higher at bottom than on surface.

Meanwhile, 3D ToF-SIMS mapping images were also obtained to show the distribution of donor and acceptor in the vertical direction (Figure 5e–j). These images again proved the acceptor enrichment on ZnO surface for the SC films.

In contrast, acceptor and donor uniformly distributed in the printed film. According to these results, the schematic diagram of vertical phase separation in the SC and IJP films was described in Figure 5k,l. The surface composition of the coated and printed films was also proved by the contact angle results (Figure S7, Supporting Information), from which the surface components were estimated according to the Cassie's equation (Equation (1)).^[19,30,56]

$$\cos \theta_{\text{blend}} = \sigma_{\text{PBDB-T}} \cos \theta_{\text{PBDB-T}} + \sigma_{\text{ITIC}} \cos \theta_{\text{ITIC}} \quad (1)$$

In this equation, $\cos \theta_{\text{blend}}$ is the cosine value of contact angle, and σ is the surface composition of donor and acceptor. As a result, the surface composition of SC films contained 83.26% PBDB-T and 16.74% ITIC. For IJP films, the surface composition contained 67.64% PBDB-T and 32.36% ITIC. The ToF-SIMS results, together with the contact angle results obviously revealed that film processing technique strongly impacted the surface components of blend films. Specifically, donor PBDB-T more easily enriched on surface of the SC films relative to the printed films.

To explain the phase separation mechanism of donor (D) and acceptor (A) in the IJP films, temperature-dependent CN/S ratio was investigated (Figure S8, Supporting Information). The observation revealed a huge influence of temperature on the vertical phase separation for the printed films. At low temperatures, we found an inhomogeneous vertical phase separation with donor rich at surface. At high temperatures, however, the CN/S ratio kept unchanged at different depths. Based on these observations, we speculated the phase separation mechanism as follow: in case of inkjet printing at high temperature, the droplets immediately dried and solidified to form dry film, remaining donor and acceptor keep homogeneously in the blend films as in the precursor solution. As a consequence, nearly no phase separation difference was observed from film surface to bottom. While during spin-coating at room temperature, the solidification process was

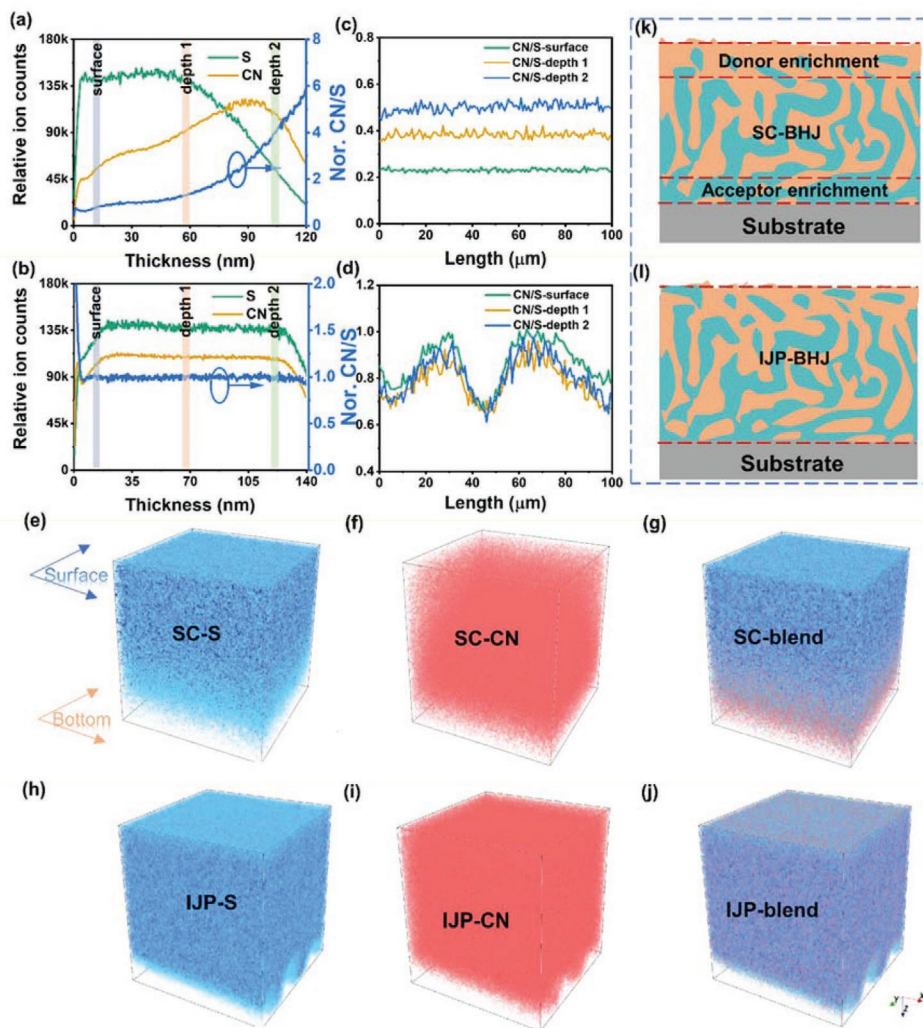


Figure 5. ToF-SIMS depth profiles of a) spin-coated films, and b) inkjet-printed films. The blue, red and green areas represent surface, depth 1 and depth 2, respectively. Intensity changes of CN, S anion and CN/S in c) coated and d) printed films perpendicular to the printing direction at different depths. 3D ToF-SIMS images of e–g) spin-coated films, and h–j) inkjet-printed films. The schematic diagram of the vertical phase separation morphology for the k) SC and l) IJP films.

slower, thereby the donor and acceptor could move for longer time. Particularly the addition of DIO additive would prolong the movement time of acceptor. Due to these reasons, bulk-heterojunction exhibited a gradient phase separation structure in the vertical direction for the SC films. Since the vertical phase separation was decided by drying speed. So, the IJP films from low temperature could form a similar gradient vertical phase separation morphology. In term of stability, the enrichment of acceptor at ZnO interface in the SC film resulted in more serious decomposition of acceptor in the SC devices relative to the IJP device, which was the reason of poorer stability for the SC devices.

2.5. Manipulation of Vertical Phase Separation by Layer-by-Layer IJP

The results demonstrated increasing temperature could reduce excessive aggregation and improve exciton separation, whereas

the homogenous vertical phase separation printed from high temperature is not ideal for charge collection. Therefore, a balanced nanophase donor: acceptor blend morphology and the vertical phase separation would be critical for further improving device performance. We then developed a layer-by-layer inkjet printing (LbL-IJP) process for the preparation of photoactive layer. **Figure 6a** is the schematic diagram of this process, where NFAs acceptors were firstly printed, polymer donors were then subsequently printed using the same printing parameters with substrate temperature around 50 °C. **Figure 6b** shows the CN/S ratio in the LbL PBDB-T:ITIC blend film (printed at 50 °C) measured by ToF-SIMS, and result indicated a gradient increase of CN/S ratio from film bottom to surface. Such a morphology firstly suggested the successful penetration of PBDB-T into the ITIC layer during the printing of polymer donor on the top of small molecular acceptor. In addition, the higher CN/S ratio at the bottom indicated that LbL-IJP route has successfully promoted the formation of a gradient vertical phase separation. Previously, LbL deposition

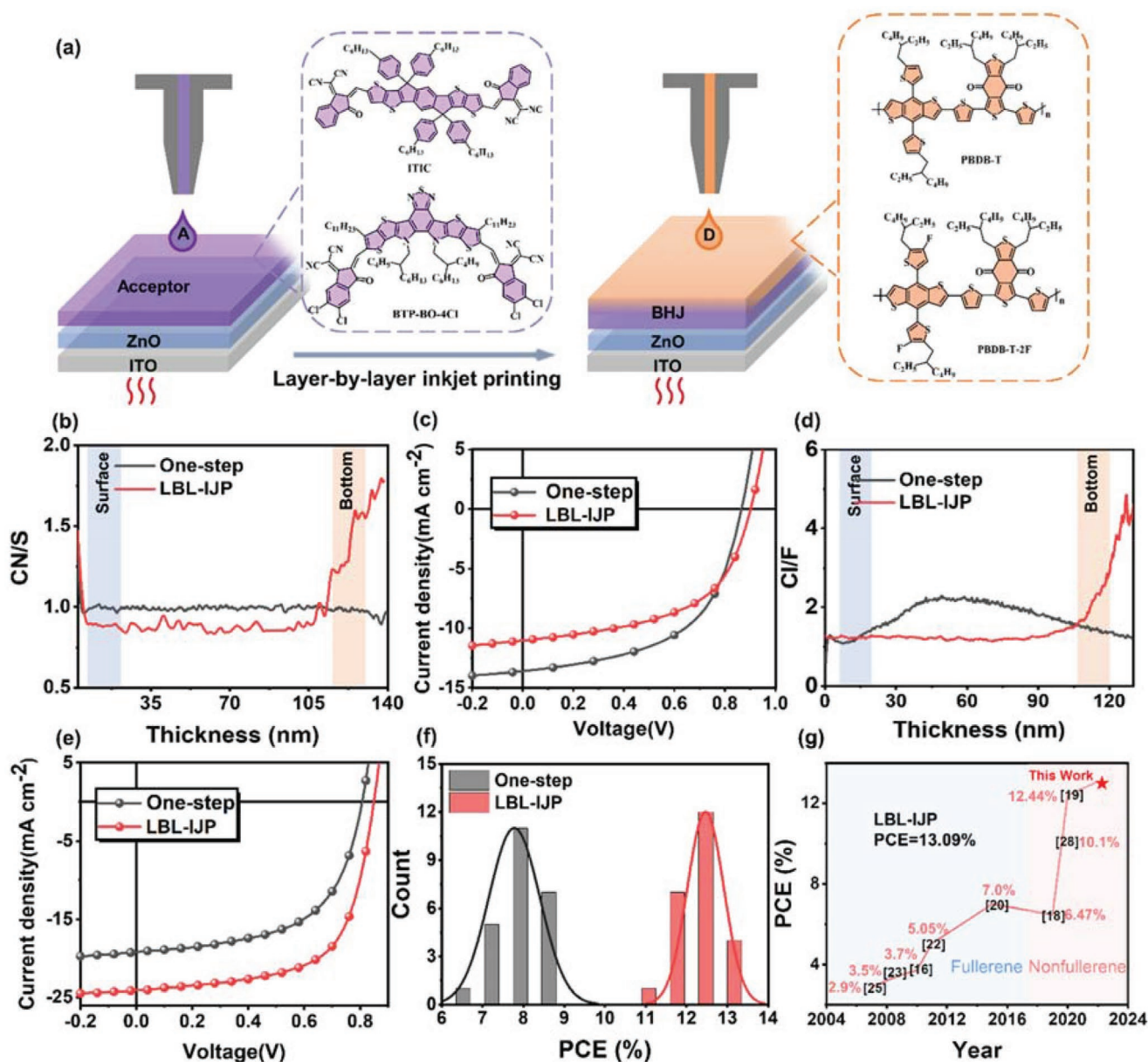


Figure 6. a) Diagram illumination of LbL-IJP process and molecular structures of donor and acceptor. b,d) ToF-SIMS images of PBDB-T:ITIC and PBDB-T-2F:BTP-BO-4Cl films from one-step and LbL-IJP, respectively. c,e) J - V characteristics of the PBDB-T:ITIC and PBDB-T-2F:BTP-BO-4Cl devices from one-step and LbL-IJP, respectively. f) The histogram of the one-step and LbL-IJP processed OSCs. g) Summary of efficiency of the inkjet-printed OSCs in recent years. (For the references of the points, more details are shown in Table S4, Supporting Information).

has been already proved to be a feasible method to regulate the vertical components both in spin-coating^[57–59] and doctor-blade coating.^[33,60] Similar gradient vertical phase separation, in some cases called “pseudo bilayer heterojunction” have been obtained in the coated films, which was beneficial for the charge collection in the cells. During IJP, both the donor and acceptor droplets were controllably deposited sequentially. Thus, the composition of the final films was theoretically decided by the precursor solution. However, in spin-coating process, the pre-coated donor or acceptor layer might be washed during the deposition of the second layer, which might make it more difficult to optimize solvent and concentration in LbL coating. Table 2 lists the per-

formance parameters of the devices with one-step IJP and LbL IJP films. Figure 6c shows the J - V curves of the PBDB-T:ITIC cells prepared by one-step IJP and LbL-IJP. PCEs of 6.43% and 5.38% were observed for these two cells. Though an appropriate vertical phase separation was obtained in the LbL films, the J_{SC} was lower than the one-step IJP devices, which could be ascribed to poorer thin film quality since ITIC was re-dissolved by oDCB during printing of donor and form excess aggregation.^[61,62] Obvious fiber morphology was found in the PBDB-T:ITIC from LbL-IJP (Figure S9, Supporting Information).

To further prove the concept of using LbL-IJP to achieve an ideal vertical phase separation, a higher efficient photoactive

Table 2. Device performance of the PBDB-T:ITIC and PBDB-T-2F:BTP-BO-4Cl OSCs from LbL-IJP process.

Active layer	Printing Method	V_{OC} (V)	J_{SC} (mA/cm ²)	FF	PCE ^{a)} (%)
PBDB-T:ITIC	One step	0.863 (0.863 ± 0.001)	13.60 (13.42 ± 0.13)	0.55 (0.54 ± 0.01)	6.43 (6.23 ± 0.20)
	LbL-IJP	0.901 (0.897 ± 0.002)	11.03 (10.69 ± 0.27)	0.54 (0.54 ± 0.01)	5.38 (5.20 ± 0.18)
PBDB-T-2F:BTP-BO-4Cl	One step	0.799 (0.799 ± 0.001)	18.68 (18.32 ± 0.33)	0.58 (0.58 ± 0.01)	8.72 (8.54 ± 0.22)
	LbL-IJP	0.850 (0.847 ± 0.002)	24.07 (23.88 ± 0.13)	0.64 (0.63 ± 0.01)	13.09 (12.96 ± 0.13)
	SC	0.831 (0.829 ± 0.002)	23.88 (23.47 ± 0.24)	0.68 (0.68 ± 0.01)	13.56 (13.42 ± 0.14)

^{a)}average PCE was calculated over eight individual devices.

system with poly[(2,6-(4,8-bis(5-(2-ethylhexyl-3-fluoro)thiophen-2-yl)-benzo[1,2-b:4,5-b']dithiophene))-alt-(5,5-(1',3'-di-2-thienyl-5',7'-bis(2-ethylhexyl) benzo [1',2'-c:4',5'-c']dithiophene-4,8-dione)] (PBDB-T-2F) as donor, and 2,2'-((2Z,2'Z)-((12,13-bis(2-butylloctyl)-3,9-diundecyl-12,13-dihydro-[1,2,5]thiadiazolo[3,4-e]thieno[2'',3''':4',5']thieno[2',3':4,5]pyrrolo [3,2-g]thieno[2',3':4,5]thieno[3,2-b]indole-2,10-diyli)bis(methanylylidene))bis(5,6-dichloro-3-oxo-2,3-dihydro-1H-indene-2,1-diyliidene)) dimalononitrile (BTP-BO-4Cl)^[63] as acceptor was tested. Before the comparison of one-step and LbL-IJP, the PBDB-T-2F:BTP-BO-4Cl films were firstly optimized through regulating the drop spacing and temperature. The optical microscope images (Figure S10, Supporting Information) and AFM images (Figure S11, Supporting Information) of the PBDB-T-2F:BTP-BO-4Cl films processed by one-step IJP at different substrate temperatures and drop spacings demonstrated the films at DS of 40 μm and temperature of 50 °C were more continuous and homogenous. In addition, the devices presented a temperature-dependent performance, which was similar to the PBDB-T:ITIC device. Specifically, device performance significantly improved from 4.52% to 8.72% when temperature increasing from 30 to 60 °C (Table S3, Supporting Information). Among the performance parameters, a great increment of J_{SC} and FF was observed. These results were in consistent with the PBDB-T:ITIC devices.

Then, the vertical phase separation of PBDB-T-2F:BTP-BO-4Cl blend films printed by one-step and LbL-IJP methods was estimated using the Cl/F ratio (Figure 6d, Table 2) from the ToF-SIMS images. It was found the intensity of Cl coming from acceptor increased at the bottom, indicating the formation of a gradient vertical phase separation structure. However, no acceptor enrichment at bottom was found in the one-step IJP film. Besides the formation of a gradient vertical phase separation, the surface ToF-SIMS mapping (Figure S12, Supporting Information) exhibited the composition distribution of donor and acceptor in the LbL-IJP films also became more homogenous as well. Negligible D/A separation difference was observed at the edge and center of the printed lines. With the one-step and LbL-IJP active layers, we fabricated inverted OSCs. As showed by the J - V characteristics (Figure 6e), the device from one-step IJP gave a performance of 8.72%. Encouragingly, the LbL-IJP device showed a significant improved efficiency of 13.09%, with V_{OC} , J_{SC} , and FF of 0.85 V, 24.07 mA cm⁻² and 64%. The performance histogram of LbL-IJP devices from 24 individual devices was shown in Figure 6f. Such a value is the highest performance for the OSCs with inkjet-printed active layer till now (as showed by Figure 6g).^[19] As a comparison, the

PBDB-T-2F:BTP-BO-4Cl devices were also fabricated through spin-coating with oDCB as solvent. Though a high efficiency of 16–17% for the PBDB-T-2F:BTP-BO-4Cl device was reported in the references.^[41,63] Herein the SC device showed a performance of 13.56% with V_{OC} of 0.83 V, J_{SC} of 23.88 mA cm⁻² and FF of 68%. The relative low performance might be attributed to different solvents and the fabrication under air environment, while the previous works were always carried out in the N₂-filled glove box with CB solvent. Among the three kinds devices, the LbL-IJP devices have an improved V_{OC} in comparison with the one-step IJP. V_{OC} of PBDB-T:ITIC LbL-IJP device was slightly lower than the SC devices, and the V_{OC} of LbL-IJP PBDB-T-2F:BTP-BO-4Cl was higher than that of SC devices. The V_{OC} variation could be also originated from morphology differences. The formation of gradient phase separation with donor and acceptor enrichment at cathode and anode interface is beneficial to reduce charge recombination.^[61,64] Min et al.^[65] also found the LbL route has yielded reduced energy loss and boosted the device performance.

3. Conclusion

In this work, the mesoscopic and nano-phase morphology of the inkjet -printed films were studied based on GIWAXS, AFM and ToF-SIMS results. Temperature-dependent mesoscopic and nano morphologies of the printed films demonstrated both the molecular aggregation and vertical phase separation were highly printing temperature-dependent. Specifically, increasing the printing temperature would suppress the molecular aggregation and enable exciton dissociation. However, high-temperature printing also led to the formation of homogenous phase separation cross over the blend film from surface to bottom, which was unlike the gradient morphology of the spin-coated films with enrichment of donor and acceptor at the film surface and bottom. To synergistically improve the vertical separation and molecular aggregation, layer-by-layer inkjet printing at high temperature was developed. Based on the morphology optimization of the printed films combining high-temperature printing and LbL-IJP, record efficiency of 13.09% was achieved for the PBDB-T-2F:BTP-BO-4Cl devices.

4. Experimental Section

Materials: Poly[(2,6-(4,8-bis(5-(2-ethylhexyl)thiophen-2-yl)benzo[1,2-b:4,5-b']dithiophene))-alt-(5,5-(1',3'-di-2-thienyl-5',7'-bis(2-ethylhexyl) benzo[1',2'-c:4',5'-c'] dithiophene-4,8-dione))] (PBDB-T), poly[(2,6-

(4,8-bis(5-(2-ethylhexyl-3-fluoro)thiophen-2-yl)-benzo[1,2-b:4,5-b']dithiophene)-alt-(5,5-(1',3'-di-2-thienyl-5',7'-bis(2-ethylhexyl)benzo[1',2'-c:4',5'-c']dithiophene-4,8-dione)) (PBDB-T-2F), 3,9-bis(2-methylene(3-(1,1-dicyanomethylene)-indanone))-5,5,11,11-tetrakis(4-hexylphenyl)-dithieno[2,3-d:2',3'-d']-s-indaceno[1,2-b:5,6-b'] dithiophene (ITIC), and 2,2'-((2Z,2'Z)-((12,13-bis(2-butyloctyl)-3,9-diundecyl-12,13-dihydro-[1,2,5]thiadiazolo[3,4-e]thieno[2'',3''':4',5']thieno[2',3':4,5]pyrrolo [3,2-g]thieno[2',3':4,5]thieno[3,2-b]indole-2,10-diyl)bis(methanylylidene))bis(5,6-dichloro-3-oxo-2,3-dihydro-1H-indene-2,1-diylidene))dimalononitrile (BTP-BO-4Cl) were purchased from Solarmer Materials Inc. DIO, and oDCB (purity >99%) were purchased from Sigma-Aldrich.

Device Fabrication: Inverted OSCs with an architecture of glass/ITO/ZnO/PBDB-T:ITIC/MoO₃/Al were manufactured. First, the ITO glasses were cleaned with deionized water, acetone and isopropanol for 30 min sequentially. Then the ITO electrodes were UV ozone treated for 40 min. After that, the ZnO electron transporting layers were deposited on the ITO glasses at 3000 rpm for 45 s by spin coating from ZnO inks,^[66] and followed by annealing at 130 °C for 30 min. Polymer donor and non-fullerene acceptor (PBDB-T:ITIC and PBDB-T-2F:BTP-BO-4Cl) were mixed and dissolved in oDCB with concentration of 10:10 mg mL⁻¹. 0.5 vol% DIO was used as additive. The solutions were stirred at 60 °C for 2 h. The 140 nm-thick PBDB-T:ITIC films and 130 nm-thick PBDB-T-2F:BTP-BO-4Cl films were printed using Fujifilm Dimatix DMP 2850 printer with DMP printing head (16 nozzles) on ZnO films in air and annealed in the glove box. The applied voltage and meniscus pressure in the print head were set as 22 V and 5 mbar during printing. The drop spacing changed from 20 to 60 μm, and the substrate temperature changed from 30 to 60 °C. For the LbL-IJP, same applied voltage and meniscus pressure were applied. For layer-by-layer printing, donor and acceptor were dissolved in oDCB separately, and printed on ZnO sequentially with a first acceptor layer and a second donor layer. After printing, the films were annealed at 150 °C for 10 min. For the comparison, the blend layers were spin coated at 1000 rpm for 50 s. Finally, 30 nm MoO₃ and 200 nm Al were deposited on the top of the active layers successively via thermally evaporation at 1 × 10⁻⁴ Pa through a shadow mask. The effective areas of the devices are 0.09 cm².

Characterization: The rheological characteristics of the solutions was tested using rotational rheometer (Kinexus Lab of Malvern, UK). Surface tension was measured by dynamic surface tension-meter (Ez-Pi plus of Kibron Inc, Finland) at room temperature. The absorption spectra of the films were measured by a Lambda 750 UV/vis/NIR spectrophotometer (PerkinElmer). AFM images were measured by the Park XE-120 microscope on tapping mode (NSC18, Mikromasch, Tallinn, Estonia). GIWAXS measurements were characterized by the Xeuss SAXS/WAXS 3.0 system with an X-ray wavelength of 1.341 Å. (Xenocs, France). TOF-SIMS mapping of the active layers was obtained using a ToF-SIMS5-100. The current density–voltage (*J*–*V*) measurements were measured with a Keithley 2400 source meter under 100 mW cm⁻² AM 1.5 G simulated solar light (Zolix SS150) in a nitrogen glove box. EQE spectrum was characterized using a halogen lamp (Osram 64610), a monochromator (Zolix, Omni-λ300), and a lock-in amplifier. The long-term stability of the devices was recorded through period *J*–*V* sweeps under the condition, which was in accordance with ISOS-L-1 standard.^[67] In detail, the device was put under continuous illumination in the N₂-filled glove box using a multi-channel solar cells decay test system (PVL-T-G8001M, Suzhou D&R Instruments Co. Ltd.) with white LED light as the lamp source. The illumination light intensity was initially set so the output short-circuit current density (*J*_{SC}) is as same as that measured under standard conditions by AM1.5G. For monitoring changes in illumination light intensity, it was monitored by a photodiode (Hamamatsu S1336-8BQ). *J*–*V* characters of the devices were checked periodically, and the photovoltaic performances data (*V*_{OC}, *J*_{SC}, FF, and PCE) were calculated automatically according to the *J*–*V* curves. When *J*–*V* was tested, an external load matching the maximum power output point (*R*_{mpp} = *V*_{max}/*I*_{max}), was attached to the cell. So, the performance of devices can be recorded automatically with time to monitor the *J*–*V* curves. Because external load can change with the *J*–*V* results, the measured performance decay curves mean the performance decay behavior of cells under real operation.

Supporting Information

Supporting Information is available from the Wiley Online Library or from the author.

Acknowledgements

This work was supported by Youth Innovation Promotion Association, CAS (2019317), the National Natural Science Foundation of China (22135001, 51773224, 22075315), and CAS-CSIRO joint project (GJHZ2092-019) of Chinese Academy of Sciences, Vacuum Interconnected Nanotech Workstation, Suzhou Institute of Nano-Tech and Nano-Bionics of Chinese Academy of Sciences (CAS) (A2107).

Conflict of Interest

The authors declare no conflict of interest.

Data Availability Statements

The data that support the findings of this study are available in the supplementary material of this article.

Keywords

inkjet printing, layer-by layer deposition, nanophase separation, non-fullerene acceptors, organic solar cells

Received: January 5, 2022

Published online:

- [1] Z. He, B. Xiao, F. Liu, H. Wu, Y. Yang, S. Xiao, C. Wang, T. P. Russell, Y. Cao, *Nat. Photonics* **2015**, *9*, 174.
- [2] Y. Han, H. Dong, W. Pan, B. Liu, X. Chen, R. Huang, Z. Li, F. Li, Q. Luo, J. Zhang, Z. Wei, C. Q. Ma, *ACS Appl. Mater. Interfaces* **2021**, *13*, 17869.
- [3] Z. Wang, Y. Han, L. Yan, C. Gong, J. Kang, H. Zhang, X. Sun, L. Zhang, J. Lin, Q. Luo, C. Q. Ma, *Adv. Funct. Mater.* **2020**, *31*, 2007276.
- [4] H. Zhen, K. Li, Y. Zhang, L. Chen, L. Niu, X. Wei, X. Fang, P. You, Z. Liu, D. Wang, F. Yan, Z. Zheng, *J. Semicond.* **2018**, *39*, 014002.
- [5] Q. Liu, Y. Jiang, K. Jin, J. Qin, J. Xu, W. Li, J. Xiong, J. Liu, Z. Xiao, K. Sun, S. Yang, X. Zhang, L. Ding, *Sci. Bull.* **2020**, *65*, 272.
- [6] M. Zhang, L. Zhu, G. Zhou, T. Hao, C. Qiu, Z. Zhao, Q. Hu, B. W. Larson, H. Zhu, Z. Ma, Z. Tang, W. Feng, Y. Zhang, T. P. Russell, F. Liu, *Nat. Commun.* **2021**, *12*, 309.
- [7] Z. Chen, W. Song, K. Yu, J. Ge, J. Zhang, L. Xie, R. Peng, Z. Ge, *Joule* **2021**, *5*, 2395.
- [8] J. Wang, Z. Zheng, Y. Zu, Y. Wang, X. Liu, S. Zhang, M. Zhang, J. Hou, *Adv. Mater.* **2021**, *33*, 2102787.
- [9] T. Zhang, C. An, P. Bi, Q. Lv, J. Qin, L. Hong, Y. Cui, S. Zhang, J. Hou, *Adv. Energy Mater.* **2021**, *11*, 2101705.
- [10] Y. Cui, Y. Xu, H. Yao, P. Bi, L. Hong, J. Zhang, Y. Zu, T. Zhang, J. Qin, J. Ren, Z. Chen, C. He, X. Hao, Z. Wei, J. Hou, *Adv. Mater.* **2021**, *33*, 2102420.
- [11] Y. Lin, Y. Jin, S. Dong, W. Zheng, J. Yang, A. Liu, F. Liu, Y. Jiang, T. P. Russell, F. Zhang, F. Huang, L. Hou, *Adv. Energy Mater.* **2018**, *8*, 1701942.

- [12] S. K. Karunakaran, G. M. Arumugam, W. Yang, S. Ge, S. N. Khan, X. Lin, G. Yang, *J. Mater. Chem. A* **2019**, *7*, 13873.
- [13] S. Ganesan, S. Mehta, D. Gupta, *Opto-Electron. Rev.* **2019**, *27*, 298.
- [14] P. Maisch, K. C. Tam, L. Lucera, H.-J. Egelhaaf, H. Scheiber, E. Maier, C. J. Brabec, *Org. Electron.* **2016**, *38*, 139.
- [15] Y. Galagan, E. W. C. Coenen, S. Sabik, H. H. Gorter, M. Barink, S. C. Veenstra, J. M. Kroon, R. Andriessen, P. W. M. Blom, *Sol. Energy Mater. Sol. Cells* **2012**, *104*, 32.
- [16] S. H. Eom, H. Park, S. H. Mujawar, S. C. Yoon, S. S. Kim, S. I. Na, S. J. Kang, D. Khim, D. Y. Kim, S. H. Lee, *Org. Electron.* **2010**, *11*, 1516.
- [17] A. Sacramento, M. Ramirez-Corno, V. S. Balderrama, S. I. Garduno, M. Estrada, L. F. Marsal, *IEEE J. Electron Devices Soc.* **2020**, *8*, 413.
- [18] D. Corzo, K. Almasabi, E. Bihar, S. Macphee, D. Rosas-Villalva, N. Gasparini, S. Inal, D. Baran, *Adv. Mater. Technol.* **2019**, *4*, 1900040.
- [19] D. Corzo, E. Bihar, E. B. Alexandre, D. Rosas-Villalva, D. Baran, *Adv. Funct. Mater.* **2020**, *31*, 2005763.
- [20] T. M. Eggenhuisen, Y. Galagan, A. F. K. V. Biezemans, T. M. W. L. Slaats, W. P. Voorthuijzen, S. Kommeren, S. Shanmugam, J. P. Teunissen, A. Hadipour, W. J. H. Verhees, S. C. Veenstra, M. J. J. Coenen, J. Gilot, R. Andriessen, W. A. Groen, *J. Mater. Chem. A* **2015**, *3*, 7255.
- [21] E. Bihar, D. Corzo, T. C. Hidalgo, D. Rosas-Villalva, K. N. Salama, S. Inal, D. Baran, *Adv. Mater. Technol.* **2020**, *5*, 2000226.
- [22] S. Jung, A. Sou, K. Banger, D.-H. Ko, P. C. Y. Chow, C. R. McNeill, H. Sirringhaus, *Adv. Energy Mater.* **2014**, *4*, 1400432.
- [23] K. Y. Mitra, A. Alalawe, S. Voigt, C. Boeffel, R. R. Baumann, *Micromachines* **2018**, *9*, 642.
- [24] H. Jinno, T. Yokota, M. Koizumi, W. Yukita, M. Saito, I. Osaka, K. Fukuda, T. Someya, *Nat. Commun.* **2021**, *12*, 2234.
- [25] N. Cui, Y. Song, C. H. Tan, K. Zhang, X. Y. Yang, S. Dong, B. M. Xie, F. Huang, *npj Flex. Electron.* **2021**, *5*, 31.
- [26] C. N. Hoth, S. A. Choulis, P. Schilinsky, C. J. Brabec, *J. Mater. Chem.* **2009**, *19*, 5398.
- [27] V. Marin, E. Holder, M. M. Wienk, E. Tekin, D. Kozodaev, U. S. Schubert, *Macromol. Rapid Commun.* **2005**, *26*, 319.
- [28] C. N. Hoth, S. A. Choulis, P. Schilinsky, C. J. Brabec, *Adv. Mater.* **2007**, *19*, 3973.
- [29] A. Teichler, R. Eckardt, S. Hoepfener, C. Friebe, J. Perelaer, A. Senes, M. Morana, C. J. Brabec, U. S. Schubert, *Adv. Energy Mater.* **2011**, *1*, 105.
- [30] P. Perkhun, W. Köntges, F. Pourcin, D. Esteouille, E. Barulina, N. Yoshimoto, P. Pierron, O. Margeat, C. Videlot-Ackermann, A. K. Bharwal, D. Duché, C. R. Herrero, C. Gonzales, A. Guerrero, J. Bisquert, R. R. Schröder, M. Pfannmöller, S. Ben Dkhil, J.-J. Simon, J. Ackermann, *Adv. Energy Sustainability Res.* **2021**, *2*, 2000086.
- [31] H. Zhao, H. B. Naveed, B. Lin, X. Zhou, J. Yuan, K. Zhou, H. Wu, R. Guo, M. A. Scheel, A. Chumakov, S. V. Roth, Z. Tang, P. Müller-Buschbaum, W. Ma, *Adv. Mater.* **2020**, *32*, 2002302.
- [32] H. Chen, R. Zhang, X. Chen, G. Zeng, L. Kobera, S. Abbrent, B. Zhang, W. Chen, G. Xu, J. Oh, S.-H. Kang, S. Chen, C. Yang, J. Brus, J. Hou, F. Gao, Y. Li, Y. Li, *Nat. Energy* **2021**, *6*, 1045.
- [33] R. Sun, Q. Wu, J. Guo, T. Wang, Y. Wu, B. Qiu, Z. Luo, W. Yang, Z. Hu, J. Guo, M. Shi, C. Yang, F. Huang, Y. Li, J. Min, *Joule* **2020**, *4*, 407.
- [34] Y. Zhang, K. Liu, J. Huang, X. Xia, J. Cao, G. Zhao, P. W. K. Fong, Y. Zhu, F. Yan, Y. Yang, X. Lu, G. Li, *Nat. Commun.* **2021**, *12*, 4815.
- [35] L. Zhang, X. Xu, B. Lin, H. Zhao, T. Li, J. Xin, Z. Bi, G. Qiu, S. Guo, K. Zhou, X. Zhan, W. Ma, *Adv. Mater.* **2018**, *30*, 1805041.
- [36] B. Lin, X. Zhou, H. Zhao, J. Yuan, K. Zhou, K. Chen, H. Wu, R. Guo, M. A. Scheel, A. Chumakov, S. V. Roth, Y. Mao, L. Wang, Z. Tang, P. Müller-Buschbaum, W. Ma, *Energy Environ. Sci.* **2020**, *13*, 2467.
- [37] L. Ye, H. Hu, M. Ghasemi, T. Wang, B. A. Collins, J.-H. Kim, K. Jiang, J. H. Carpenter, H. Li, Z. Li, T. McAfee, J. Zhao, X. Chen, J. L. Y. Lai, T. Ma, J.-L. Bredas, H. Yan, H. Ade, *Nat. Mater.* **2018**, *17*, 253.
- [38] H. Li, C. Zhang, J. Wei, K. Huang, X. Guo, Y. Yang, S. So, Q. Luo, C.-Q. Ma, J. Yang, *Flex. Print. Electron.* **2019**, *4*, 044007.
- [39] Y. Wang, X. Wang, B. Lin, Z. Bi, X. Zhou, H. B. Naveed, K. Zhou, H. Yan, Z. Tang, W. Ma, *Adv. Energy Mater.* **2020**, *10*, 2000826.
- [40] S. Dong, K. Zhang, T. Jia, W. Zhong, X. Wang, F. Huang, Y. Cao, *EcoMat* **2019**, *1*, e12006.
- [41] X. Zhang, J. Cai, C. Guo, D. Li, B. Du, Y. Zhuang, S. Cheng, L. Wang, D. Liu, T. Wang, *Small* **2021**, *17*, 2102558.
- [42] Y. Yan, X. Liu, T. Wang, *Adv. Mater.* **2017**, *29*, 1601674.
- [43] S. Sumaiya, K. Kardel, A. El Shahat, *Technologies* **2017**, *5*, 53.
- [44] F. C. Spano, C. Silva, *Annu. Rev. Phys. Chem.* **2014**, *65*, 477.
- [45] W. Li, M. Chen, J. Cai, E. L. K. Spooner, H. Zhang, R. S. Gurney, D. Liu, Z. Xiao, D. G. Lidzey, L. Ding, T. Wang, *Joule* **2019**, *3*, 819.
- [46] A. L. Patterson, *Phys. Rev.* **1939**, *56*, 978.
- [47] W. C. Zhao, D. P. Qian, S. Q. Zhang, S. S. Li, O. Inganas, F. Gao, J. H. Hou, *Adv. Mater.* **2016**, *28*, 4734.
- [48] D. H. Li, X. Zhang, D. Liu, T. Wang, *J. Mater. Chem. A* **2020**, *8*, 15607.
- [49] G. Feng, J. Li, Y. He, W. Zheng, J. Wang, C. Li, Z. Tang, A. Osvet, N. Li, C. J. Brabec, Y. Yi, H. Yan, W. Li, *Joule* **2019**, *3*, 1765.
- [50] Y. Chen, S. Wang, L. Xue, Z. Zhang, H. Li, L. Wu, Y. Wang, F. Li, F. Zhang, Y. Li, *J. Mater. Chem. A* **2016**, *4*, 19189.
- [51] B. Liu, Y. Han, Z. Li, H. Gu, L. Yan, Y. Lin, Q. Luo, S. Yang, C.-Q. Ma, *Sol. RRL* **2020**, *5*, 2000638.
- [52] Y. Che, M. R. Niazi, R. Izquierdo, D. F. Perepichka, *Angew. Chem. Int. Ed.* **2021**, *60*, 24833.
- [53] X. Wang, L. Zhang, L. Hu, Z. Xie, H. Mao, L. Tan, Y. Zhang, Y. Chen, *Adv. Funct. Mater.* **2021**, *31*, 2102291.
- [54] D. F. Zhang, W. K. Zhong, L. Ying, B. B. Fan, M. J. Li, Z. Q. Gan, Z. M. Zeng, D. C. Chen, N. Li, F. Huang, Y. Cao, *Nano Energy* **2021**, *85*, 105957.
- [55] J. Lv, H. Tang, J. Huang, C. Yan, K. Liu, Q. Yang, D. Hu, R. Singh, J. Lee, S. Lu, G. Li, Z. Kan, *Energy Environ. Sci.* **2021**, *14*, 3044.
- [56] A. B. D. Cassie, *Discuss. Faraday Soc.* **1948**, *3*, 11.
- [57] K. Jiang, J. Zhang, Z. Peng, F. Lin, S. Wu, Z. Li, Y. Chen, H. Yan, H. Ade, Z. Zhu, A. K. Jen, *Nat. Commun.* **2021**, *12*, 468.
- [58] M. Li, Q. Wang, J. Liu, Y. Geng, L. Ye, *Mater. Chem. Front.* **2021**, *5*, 4851.
- [59] Q. Liao, B. Li, H. Sun, C. W. Koh, X. Zhang, B. Liu, H. Y. Woo, X. Guo, *Mater. Reports: Energy* **2021**, *1*, 100063.
- [60] Y. N. Zheng, R. Sun, M. Zhang, Z. H. Chen, Z. X. Peng, Q. Wu, X. X. Yuan, Y. Yu, T. Wang, Y. Wu, X. T. Hao, G. H. Lu, H. Ade, J. Min, *Adv. Energy Mater.* **2021**, *11*, 2102135.
- [61] Y. Wei, J. Yu, L. Qin, H. Chen, X. Wu, Z. Wei, X. Zhang, Z. Xiao, L. Ding, F. Gao, H. Huang, *Energy Environ. Sci.* **2021**, *14*, 2314.
- [62] L. Huang, P. Jiang, Y. Zhang, L. Zhang, Z. Yu, Q. He, W. Zhou, L. Tan, Y. Chen, *ACS Appl. Mater. Interfaces* **2019**, *11*, 26213.
- [63] Y. Cui, H. Yao, L. Hong, T. Zhang, Y. Tang, B. Lin, K. Xian, B. Gao, C. An, P. Bi, W. Ma, J. Hou, *Natl. Sci. Rev.* **2020**, *7*, 1239.
- [64] Y. F. Wang, X. W. Zhan, *Adv. Energy Mater.* **2016**, *6*, 1600414.
- [65] R. Sun, J. Guo, C. Sun, T. Wang, Z. Luo, Z. Zhang, X. Jiao, W. Tang, C. Yang, Y. Li, J. Min, *Energy Environ. Sci.* **2019**, *12*, 384.
- [66] W. Pan, Y. Han, Z. Wang, C. Gong, J. Guo, J. Lin, Q. Luo, S. Yang, C.-Q. Ma, *J. Mater. Chem. A* **2021**, *9*, 16889.
- [67] M. O. Reese, S. A. Gevorgyan, M. Jørgensen, E. Bundgaard, S. R. Kurtz, D. S. Ginley, D. C. Olson, M. T. Lloyd, P. Morvillo, E. A. Katz, A. Elschner, O. Haillant, T. R. Currier, V. Shrotriya, M. Hermenau, M. Riede, K. R. Kirov, G. Trimmel, T. Rath, O. Inganäs, F. Zhang, M. Andersson, K. Tvingstedt, M. Lira-Cantu, D. Laird, C. McGuinness, S. Gowrisanker, M. Pannone, M. Xiao, J. Hauch, et al., *Sol. Energy Mater. Sol. Cells* **2011**, *95*, 1253.